Proton Transfer Mediator Boosting the Current Density of Biomass Electrooxidation to Ampere-Level

Zhaohui Yang,[a] Shao Wang,[a] Chenyang Wei,[a] Lan Chen,[b] Zhimin Xue,*[b]

Tiancheng Mu*[a]

a Dr. Z. Yang, S. Wang, Dr. C. Wei, and Prof. T. Mu

Department of Chemistry, Renmin University of China, Beijing 100872, China. E-mail: tcmu@ruc.edu.cn

b Dr. L. Chen, Prof. Z. Xue

Beijing Key Laboratory of Lignocellulosic Chemistry, College of Materials Science and Technology, Beijing Forestry University, Beijing 100083, China. E-mail: zmxue@bjfu.edu.cn

EXPERIMENTAL SECTION

Materials: Nickel chloride hexahydrate (98%, Innochem), ruthenium chloride (97% Ru (47%), Aladdin), ammonium fluoride (98%, Aladdin), urea (99%, Innochem), sodium dihydrogen phosphate (99%, Aladdin), 5-Hydroxymethylfurfural (99%, Aladdin), 2,5-furandicarboxaldehyde (98%, Innochem), 5-formylfuran-2-carboxylic acid (98%, Innochem), 5-hydroxymethyl- 2-furancarboxylic acid (98%, Innochem), 2,5-Furandicarboxylic acid (99%, Innochem), Methanol (99.9%, Innochem), ammonium formate (99%, Aladdin), ethanol (99.7%, SCR), acetone (99.5%, Acros), milli-Q water (18.2 MΩ), nickel foam (MTI) were used without further purification.

Preparation of electrode: A piece of nickel foam (2 × 3 cm^2) was cleaned by acetone, 3 M HCl ethanol and DI water for 10 min, respectively. 0.594g $NiCl_2 \cdot 6H_2O$, 0.148g NH_4F, 0.6g $CO(NH_2)_2$ were mixed in 30 ml DI water, after magnetic stirring for 30 min, the solution was transferred into a 50 ml Teflon-lined autoclave where a cleaned NF vertically placed into it. The autoclave was sealed and maintained at 120 ℃ for 12 h to obtain $Ni(OH)_2$/NF. To prepare PO_4/Ru-$Ni(OH)_2$/NF, 15 ml 6 mM $RuCl_3$ solution was mixed with 15 ml 0.1 M NaH_2PO_4 solution in a 50 ml autoclave, then a $Ni(OH)_2$/NF was transferred into it. After sealing, the autoclave was heated to 140 ℃ for 4 h to obtain PO_4/Ru-$Ni(OH)_2$/NF. The mass loading of PO_4/Ru-$Ni(OH)_2$ on Ni foam was ~3.2 mg cm^{-2}. PO_4/$Ni(OH)_2$/NF and Ru-$Ni(OH)_2$/NF were synthesized by the same method without $RuCl_3$ and NaH_2PO_4, respectively.

Electrochemical measurements: The electrochemical performances were tested by a CS350M workstation with standard three-electrode system consisting of as-prepared electrodes (1 × 1 cm^2) as working electrode, a carbon rod and Hg/HgO were used as counter and reference electrode, respectively. All tests were performed in H-type cell with Nafion 212 membrane as the separator. The linear sweep voltammetry (LSV) was conducted at the scan rate of 5 mV s^{-1} with 90% iR correction. The electrochemically active surface area (ECSA) was obtained from the electrical double layer specific

capacitor (C_{dl}). Cyclic voltammetry (CV) measurements were conducted in a non-faradaic potential range at different scan rates from 20 to 120 mV s^{-1} to acquire C_{dl}. Electrochemical impedance spectroscopy (EIS) was measured from 0.01 to 10^5 Hz. All tests were performed in H-type cell with Nafion 212 membrane as the separator. Turnover frequency (TOF) was calculated by the equation as TOF = j / (6× n× F), where j is the current density for HMFOR, F is the Faraday constant (96485 C/mol), n is the amount of available active sites obtained by the ratio of the charge oxidized by divalent nickel to the Faraday efficiency. In-situ Raman was performed on an Xplora Plus Raman instrument with a 10x objective. Raman frequencies were firstly calibrated by Si wafer (520.6 cm^{-1}). A laser power was 1.5 mW and the lines were 638 nm. It took 30 s to obtain one spectrum each time with two accumulations. Quasi-operando Raman spectra were acquired by oxidizing $Ni(OH)_2$/NF and PO_4/Ru-$Ni(OH)_2$/NF at the potential of 1.45 V vs. RHE and then adding HMF, which was taken out after a period of reaction and the corresponding Raman spectra were measured, in which the acquisition time was shortened to 5s with one accumulation. The electrochemical signal was input through CHI 660E, and Ag/AgCl and Pt wire were used as reference electrodes and counter electrodes respectively in the Raman cell, IR compensation is 90%. Quasi-operando FTIR spectra were obtained by using PO_4/Ru-$Ni(OH)_2$/NF as an electrode reacts at different voltages for 5 min in 1 M KOH with 50 HMF, then the spectra were recorded on an FT-IR spectrometer (Tensor 27, Bruker) in the range of 4000 to 400 cm^{-1}.

XAFS Experiment and Data Processing: XAFS measurements at Ni k-edge in both transmission (for Ni foil) and fluorescence (for samples) mode were performed at Hard X-ray branch of the E-line (BL20U1) in Shanghai Synchrotron Radiation Facility (SSRF). The electron beam energy was 3.5 GeV and the stored current was 200 mA (top-up). The hard X-ray branch of energy material beamline (E-line) with a photon flux of 2×1012 photons/s (0.1%BW) at 5 keV and a beam size of 80×20 μm is generated from 24-pole in-vacuum undulators. XAFS data were collected using a fixed-exit double-crystal Si(111) monochromator. A Lytle detector was used to collect the fluorescence signal, and the energy was calibrated using Ni foil. The raw data analysis was

performed using IFEFFIT software package according to the standard data analysis procedures. The spectra were calibrated, averaged, pre-edge background subtracted, and post-edge normalized using Athena program in IFEFFIT software package. The Fourier transformation of the k^3-weighted EXAFS oscillations, $k^3 \cdot \chi(k)$, from k space to R space was performed to obtain a radial distribution function. And data fitting was done by Artemis program in IFEFFIT.

XAFS measurements at Ru k-edge were performed at the BL14W1 in Shanghai Synchrotron Radiation Facility (SSRF). The electron beam energy was 3.5 GeV and the stored current was 200 mA (top-up). A 38-pole wiggler with the maximum magnetic field of 1.2 T inserted in the straight section of the storage ring was used. XAFS data were collected using a fixed-exit double-crystal Si(111) monochromator. A Lytle detector was used to collect the fluorescence signal, and the energy was calibrated using Pt foil. The photon flux at the sample position was 2.6×1012 photons per second. The raw data analysis was performed using IFEFFIT software package according to the standard data analysis procedures. The spectra were calibrated, averaged, pre-edge background subtracted, and post-edge normalized using Athena program in IFEFFIT software package. The Fourier transformation of the k^2-weighted EXAFS oscillations, $k^2 \cdot \chi(k)$, from k space to R space was performed to obtain a radial distribution function. And data fitting was done by Artemis program in IFEFFIT.

HPLC analysis of products: HMF and its oxidation products (HMFCA, FFCA, DFF, FDCA) were analyzed by high-performance liquid chromatography (HPLC, LC3000I system with an ultraviolet-visible detector and a 4.6 mm × 250 mm AQ-C18 column). In a typical measurement, a 10 µL aliquot of electrolyte was collected during electrolytic process, diluted to 3 mL with methanol and 5 mM ammonium formate solution (3:7), and then injected into HPLC column for analysis. As for the detecting conditions, the HPLC column temperature was maintained at 35 ◦C, while the flow rate is 0.6 ml/min, and the wavelength of UV detection is 265 nm. The HMF conversion, FDCA selectivity and faradaic efficiency were calculated according to the following equations:

$$\text{HMF conversion (\%)} = n\,(\text{consumed HMF}) / n\,(\text{initial HMF}) \times 100\%$$

$$\text{FDCA selectivity (\%)} = n\,(\text{FDCA formed}) / n\,(\text{consumed HMF}) \times 100\%$$

Faradic efficiency (%) = 6 × n (FDCA formed) ×F / total charge passed × 100%

DFT calculations: All calculations were implemented in Materials Studio with the DMol^3 code. The Perdew–Burke–Ernzerhof (PBE) functional of the generalized gradient approximation (GGA) was used to calculate the exchange–correlation energy. The double numerical plus polarization (DNP) was chosen during the geometry optimization. The DFT-D method of Grimme was employed to describe the van der Waals interactions. A 20 Å vacuum layer was introduced to ensure enough region to prevent the interaction of adjacent layers. A Monkhorst-Pack k-mesh with a 3 × 3 × 1 k-point grid was used for structural optimization, while 6 × 6 × 1 for electronic structure calculations. A complete LST/QST method was used to conduct transition state search. The convergence tolerances of energy change, maximum force, and maximum displacement were set as 2×10^{-5} Ha, 0.004 Ha/Å, and 0.005 Å, respectively.

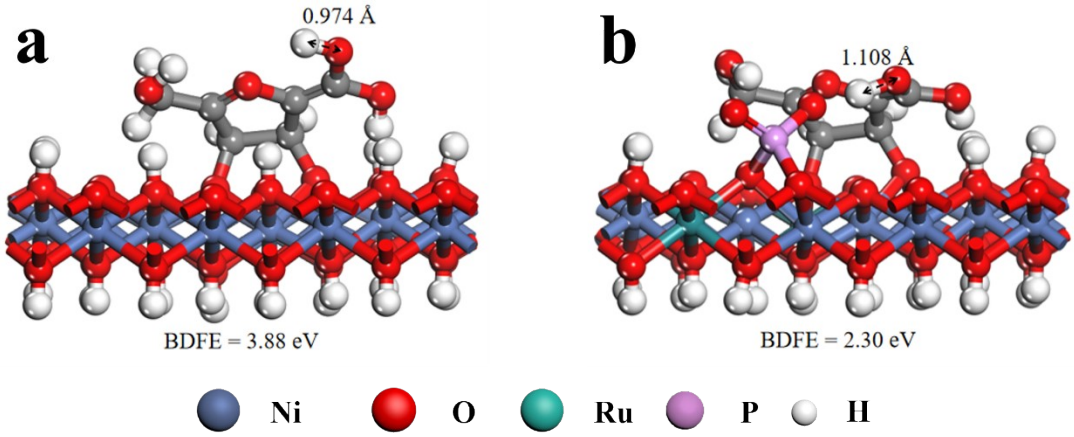

Fig. S1. O-H bond lengths as well as bond dissociation free energies (BDFE) of HMF molecules adsorbed on the surface of $Ni(OH)_2$ (a) without or (b) with phosphate modification.

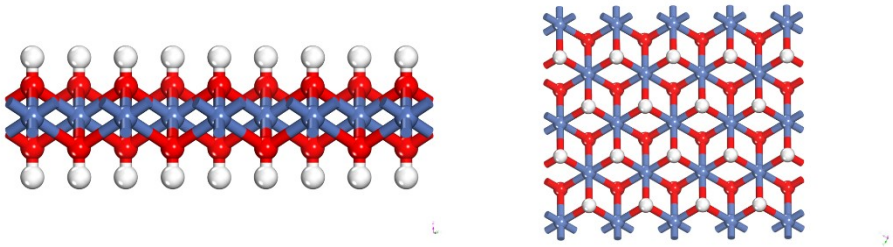

Fig. S2. The side and top view of optimized model of $Ni(OH)_2$.

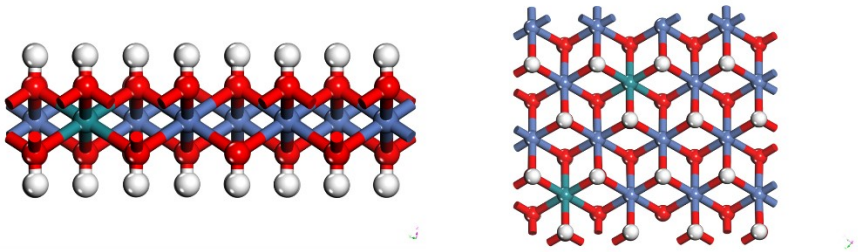

Fig. S3. The side and top view of optimized model of Ru-Ni$(OH)_2$.

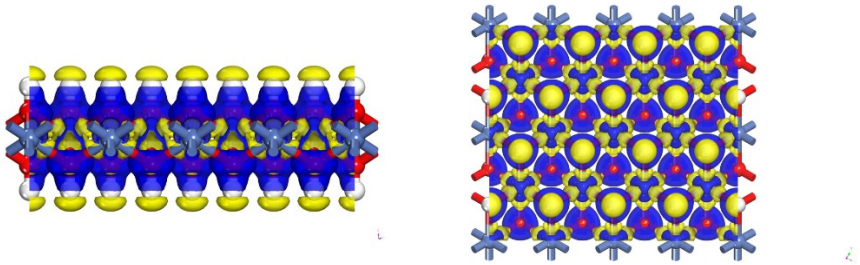

Fig. S4. The side and top view of differential charge plot of $Ni(OH)_2$.

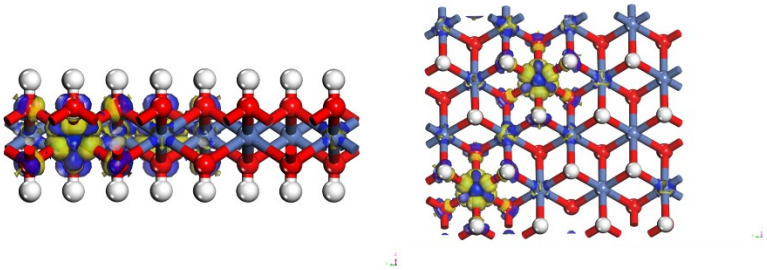

Fig. S5. The side and top view of differential charge plot of Ru-Ni$(OH)_2$.

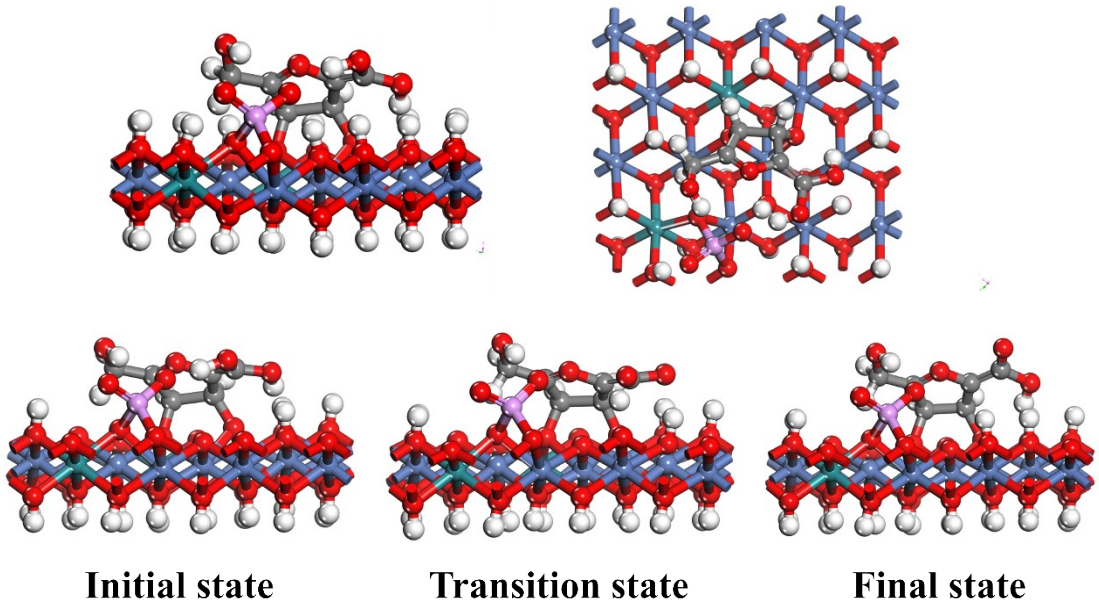

Fig. S6. The side and top view of optimized model of HMF adsorbed on PO_4/Ru-$Ni(OH)_2$ and the hydrogen transfer process.

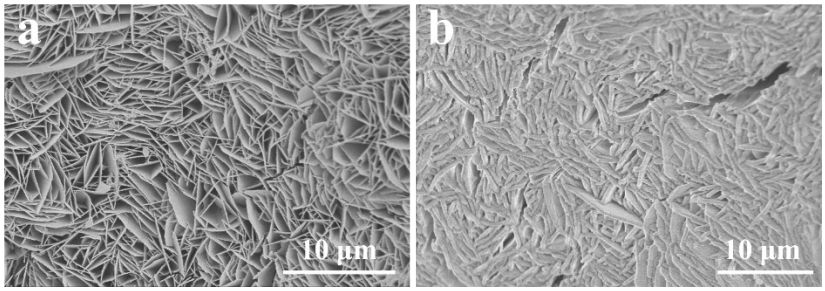

Fig. S7. SEM images of (a) Ru-$Ni(OH)_2$/NF and (b) PO_4/ $Ni(OH)_2$/NF.

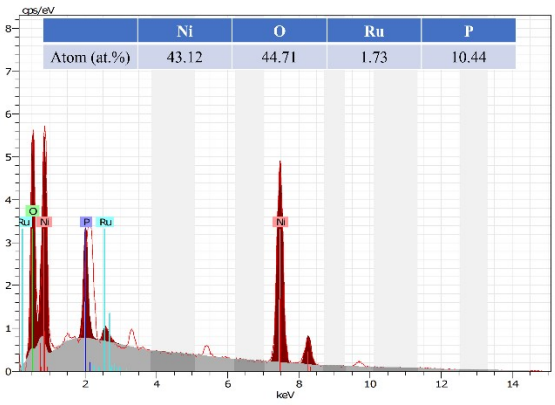

Fig. S8. Analysis of the elemental content of PO_4/ Ru-$Ni(OH)_2$/NF.

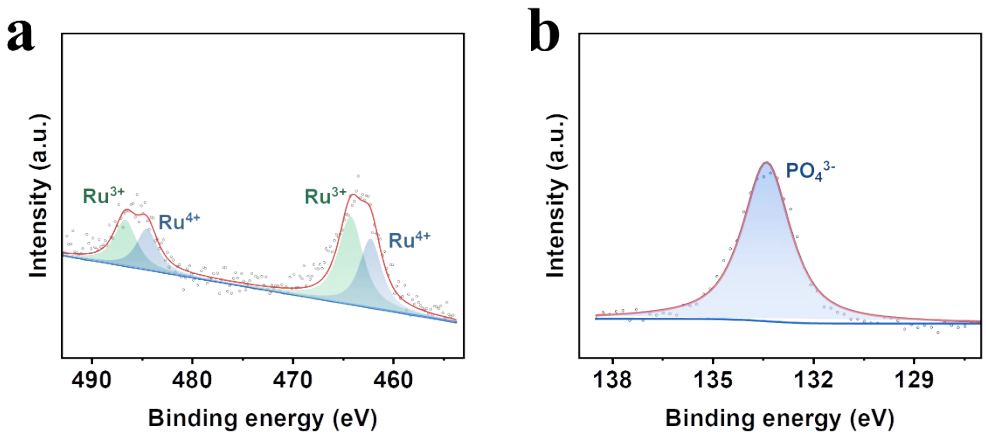

Fig. S9. high-resolution XPS pattern of (a) Ru 3p and (b) P 2p for PO_4/Ru-Ni$(OH)_2$.

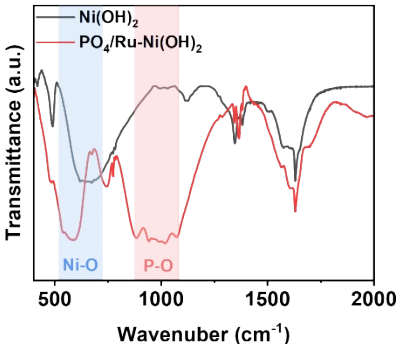

Fig. S10. FTIR spectra of PO_4/Ru-Ni$(OH)_2$ and Ni$(OH)_2$.

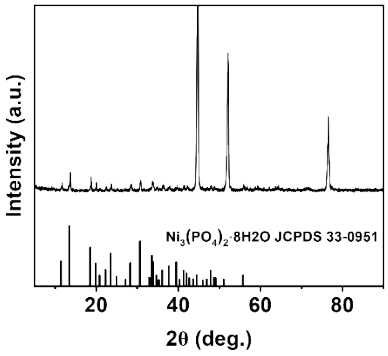

Fig. S11. The XRD spectra of the samples synthesized by increasing the amount of phosphate.

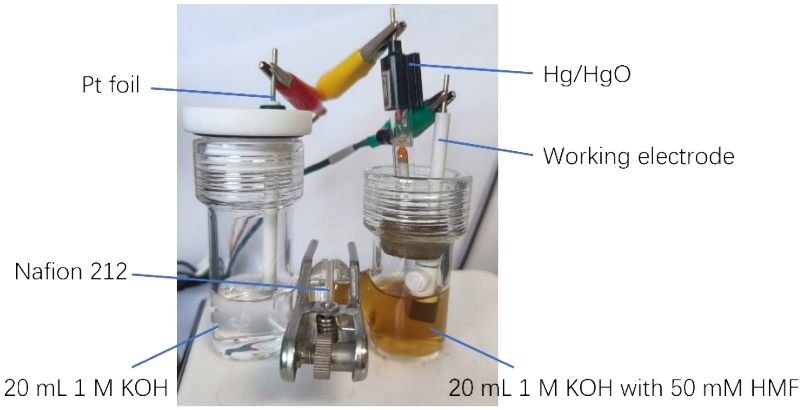

Fig. S12. Details of the electrolyzer.

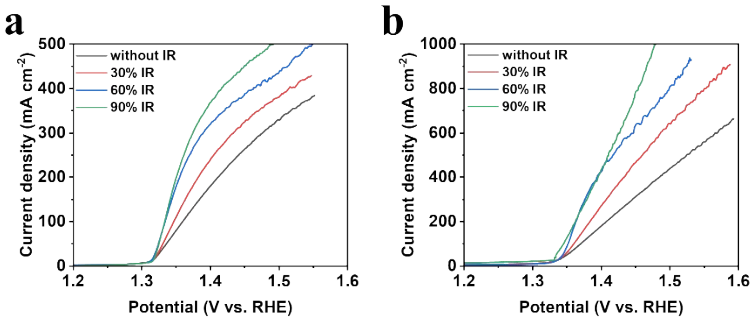

Fig. S13. LSV curves of PO_4/Ru-Ni$(OH)_2$ with different IR correction in 1 M KOH with (a) 10 mM and (b) 50 mM HMF.

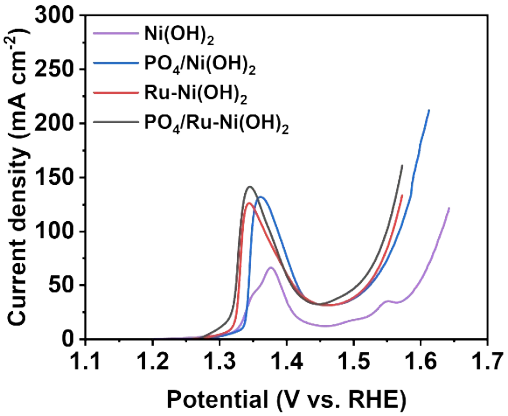

Fig. S14. LSV curves of different samples in KOH solution without HMF.

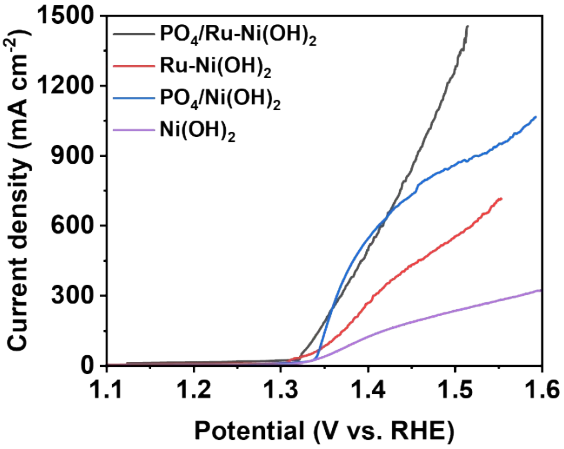

Fig. S15. LSV curves of different samples in KOH solution with 50 mM HMF.

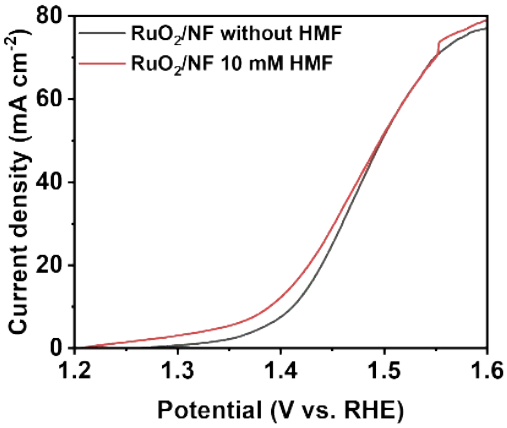

Fig.S16. LSV curves of RuO_2/NF in 1M KOH without and with 10 mM HMF.

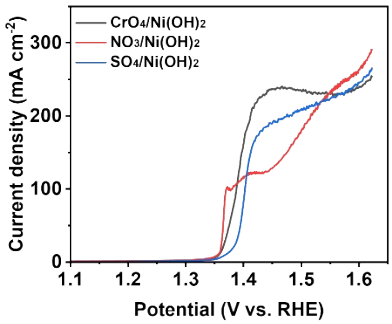

Fig. S17. LSV curves of $Ni(OH)_2$ with different acid root modified in KOH solution with 10 mM HMF.

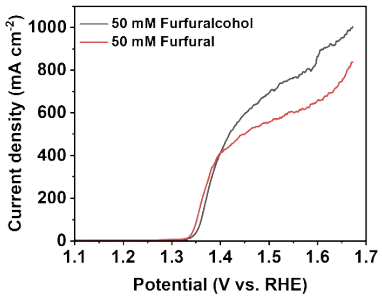

Fig. S18. LSV curves of PO_4/Ru-Ni$(OH)_2$/NF in KOH solution with 50 mM furfuralcohol and furfural.

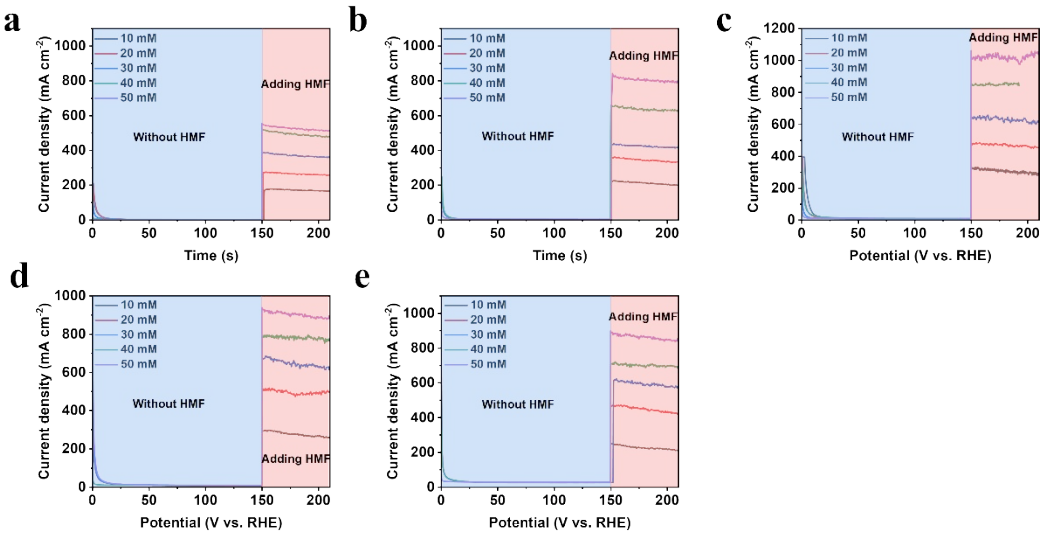

Fig. S19. Segmented i-t of PO_4/Ru-Ni$(OH)_2$/NF carried out at the potential of (a) 1.37 V, (b) 1.42 V, (c) 1.45 V, (d) 1.47 V, (e) 1.52 V.

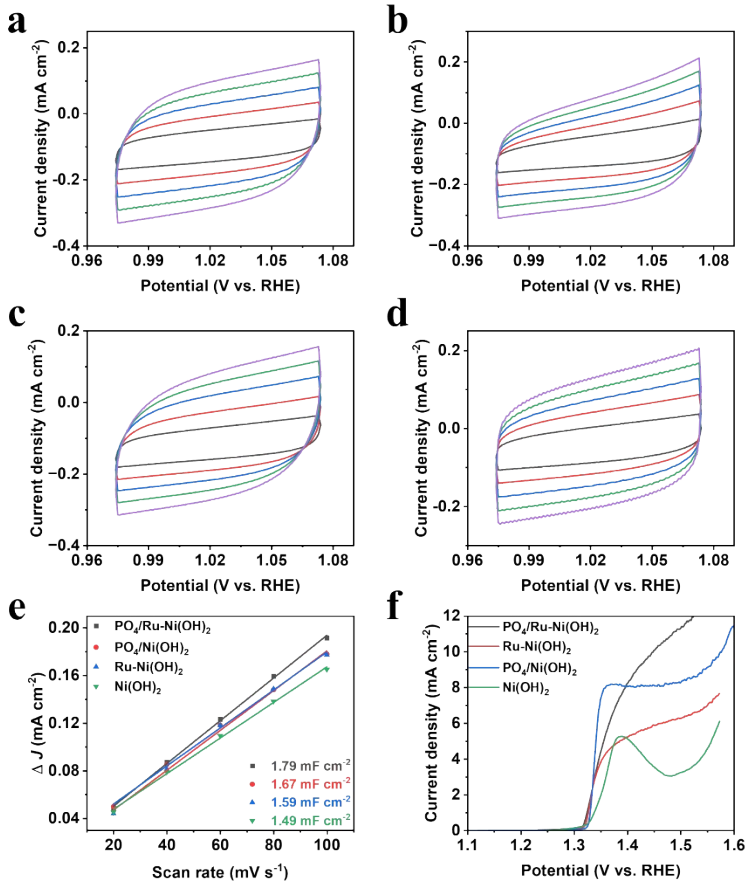

Fig. S20. CV curves of (a) PO_4/Ru-Ni$(OH)_2$/NF, (b) PO_4/ Ni$(OH)_2$/NF, (c) Ru-Ni$(OH)_2$/NF and (d) Ni$(OH)_2$/NF at different rates from 20 to 100 mV s^{-1} under the potential window of 0.97 – 1.07 V vs. RHE in 1.0 M KOH with 10 mM HMF. (e) The variation of current densities plotted against the scan rate at 1.02 V vs. RHE. (f) LSV curves normalized by ECSA.

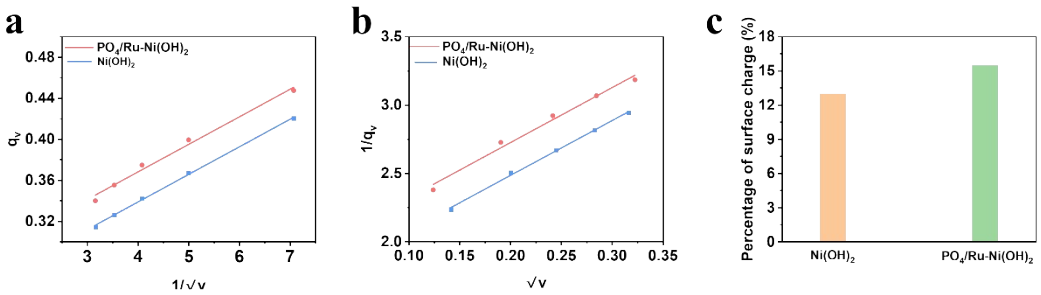

Fig. S21. Comparison of percentage of surface charge calculated by the formula: $q_v = q_e + A\frac{1}{\sqrt{v}}$, $\frac{1}{q_v} = \frac{1}{q_t} + B\sqrt{v}$, where v is the scan rate, q_v is the corresponding charge at different scan rates, q_e is the surface charge and q_t is the total charge. The charges q at different sweep speeds are calculated based on the CV plots in Fig. S13, plotted as q_v vs. $1/\sqrt{v}$ as well as $1/q_v$ vs. $\sqrt{v}$, respectively, and the intercepts of the fitted straight lines are calculated to obtain q_e as well as q_t.

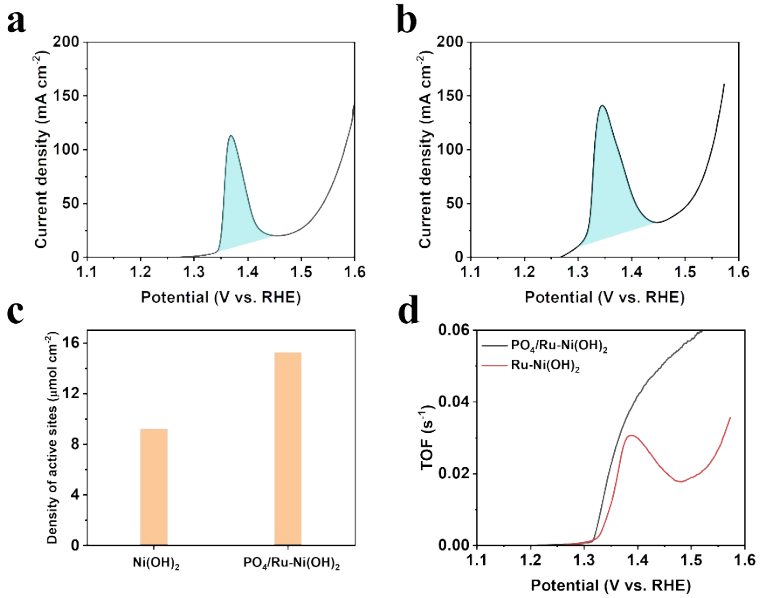

Fig. S22. LSV curves at the scan rate of 5 mV s^{-1} of (a) $Ni(OH)_2$/NF and (b) PO_4/Ru-$Ni(OH)_2$/NF in 1 M KOH without HMF. (c) Calculated density of active sites. (d) Calculated TOFs of $Ni(OH)_2$/NF and PO_4/Ru-$Ni(OH)_2$/NF for HMFOR.

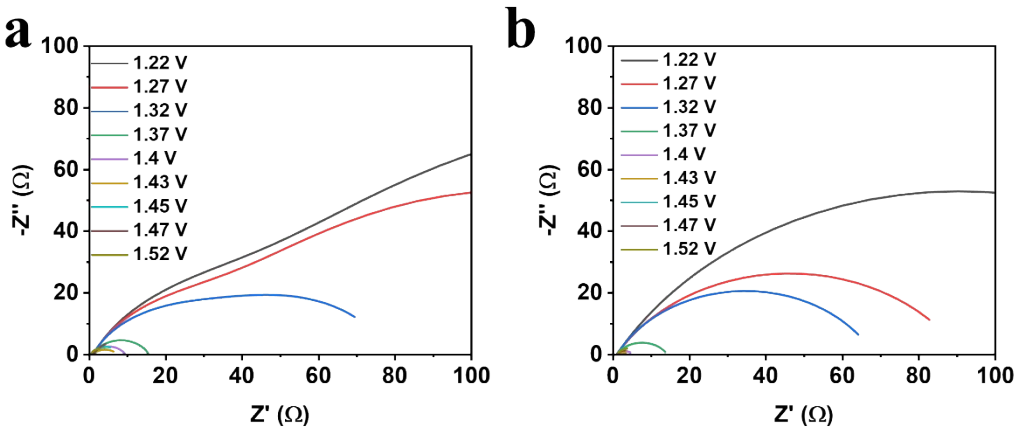

Fig. S23. Electrochemical impedance spectroscopy of (a) $Ni(OH)_2$/NF and (b) PO_4/Ru-$Ni(OH)_2$/NF at different potentials.

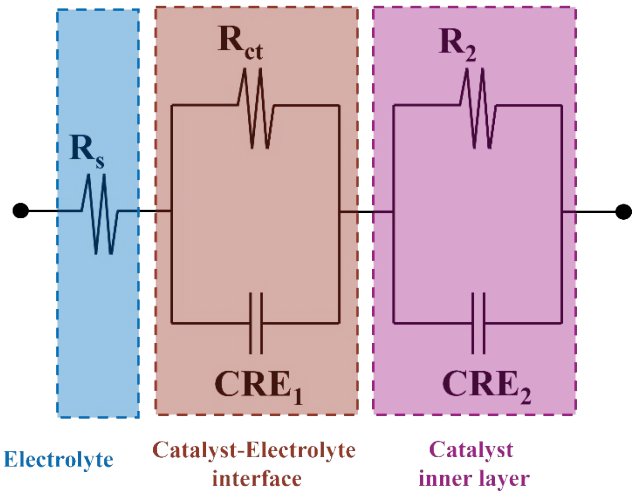

Fig. S24. The equivalent circuit image. R_s stands for the electrolyte resistance, CPE_1 represents double layer capacitance, R_{ct} has contact with the interfacial charge transfer reaction, CPE_2 and R_2 are related to the dielectric properties and the resistance of the electrode itself.

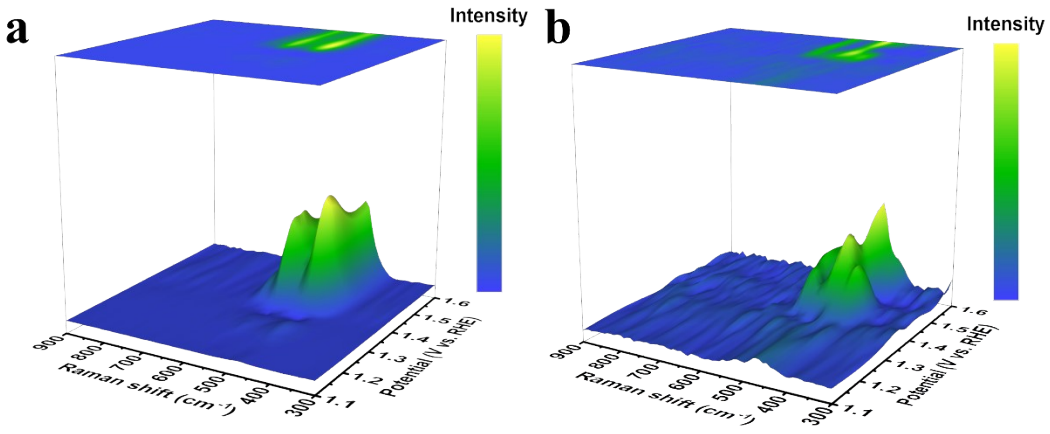

Fig. S25. In-situ Raman spectra of $Ni(OH)_2$/NF in (a) KOH solution and (b) KOH solution with 50 mM HMF.

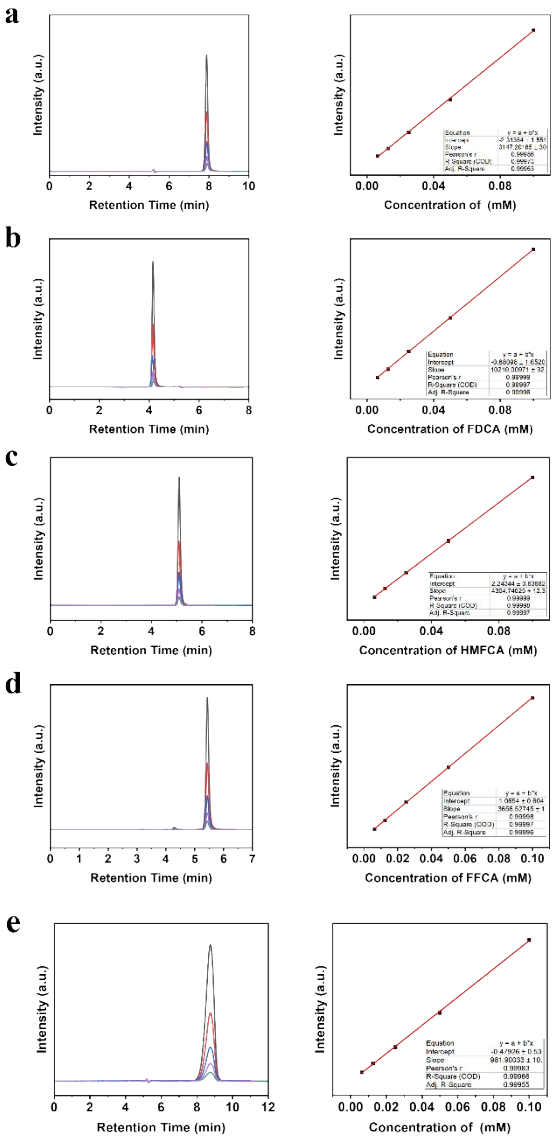

Fig. S26. Calibration of the HPLC for (a) HMF, (b) FDCA, (c) HMFCA, (d) FFCA and (e) DFF.

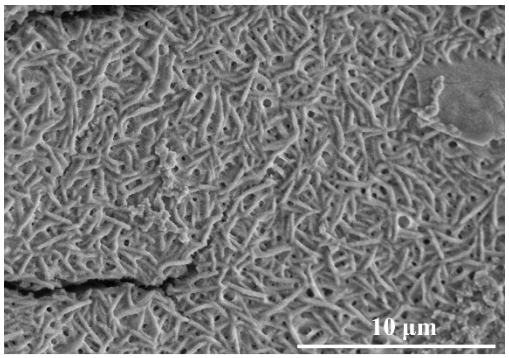

Fig. S27. SEM image of PO_4/Ru-Ni$(OH)_2$/NF after stability test.

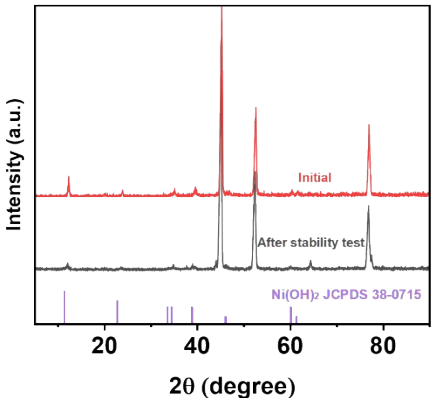

Fig. S28. XRD patterns of PO_4/Ru-Ni$(OH)_2$/NF before and after stability test.

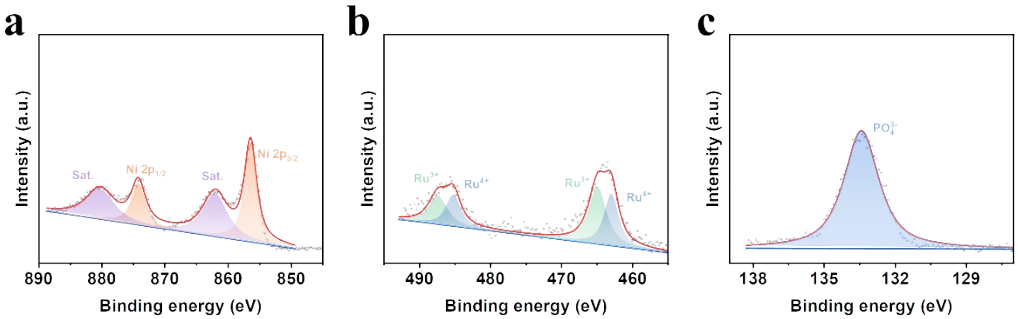

Fig. S29. High-resolution XPS spectra of PO_4/Ru-Ni$(OH)_2$/NF after stability test.

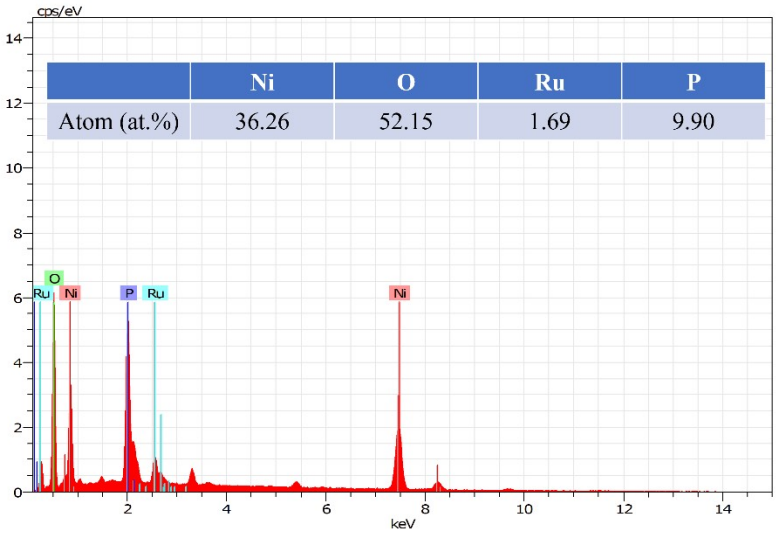

Fig. S30. Analysis of the elemental content of PO_4/ Ru-Ni$(OH)_2$/NF after stability test.

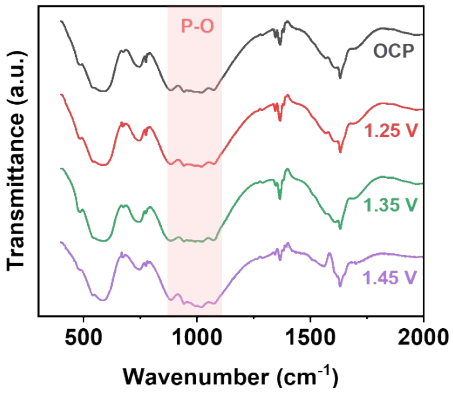

Fig. S31. quasi-in situ FT-IR measurements at various potentials for PO_4/Ru-Ni$(OH)_2$.

Table S1. Comparison of HMF electrocatalytic performance of catalysts recently reported.

Catalysts	Maximum current densities exhibited by LSV (mA cm^{-2})	Initial current densities during electrolysis (mA cm^{-2})	References
PO_4/Ru-Ni$(OH)_2$/NF	1500	1015	This work
Ni-Cu/NF	1000	300	1
Rh-O_5/Ni(Fe)	100	-	2
Co-Ni_3S_2	600	230	3
Vo-Co_3O_4	100	-	4
NiSx-NiOOH	120	20	5
FeP-$NiMoP_2$	300	85	6
lnOOH-Ov	40	12	7
CF-Cu$(OH)_2$	55	55	8
Ni_3S_2/NiOx	500	360	9
$NiCo_2O_4$	52	48	10
CoFe@NiFe	100	30	11
NiSe@NiOx	220	70	12
CoMoP	150	120	13
Ce-Co_2P@NC	100	35	14

REFERENCES

1. D. Chen, Y. Ding, X. Cao, L. Wang, H. Lee, G. Lin, W. Li, G. Ding and L. Sun, *Angew. Chem. Int. Ed.* 2023, **62**, e202309478.
2. L. Zeng, Y. Chen, M. Sun, Q. Huang, K. Sun, J. Ma, J. Li, H. Tan, M. Li, Y. Pan, Y. Liu, M. Luo, B. Huang and S. Guo, *J. Am. Chem. Soc.* 2023, **145**, 17577-17587.
3. Y. Sun, J. Wang, Y. Qi, W. Li and C. Wang, *Adv. Sci.* 2022, **9**, 2200957.
4. Y. Lu, T. Liu, C.-L. Dong, C. Yang, L. Zhou, Y.-C. Huang, Y. Li, B. Zhou, Y. Zou and S. Wang, *Adv. Mater.* 2022, **34**, 2107185.
5. C. Liu, X.-R. Shi, K. Yue, P. Wang, K. Zhan, X. Wang, B. Y. Xia and Y. Yan, *Adv. Mater.* 2023, **35**, 2211177.
6. G. Yang, Y. Jiao, H. Yan, Y. Xie, C. Tian, A. Wu, Y. Wang and H. Fu, *Nat. Commun.* 2022, **13**, 3125.
7. F. Ye, S. Zhang, Q. Cheng, Y. Long, D. Liu, R. Paul, Y. Fang, Y. Su, L. Qu, L. Dai and C. Hu, *Nat. Commun.* 2023, **14**.
8. X. Pang, H. Bai, H. Zhao, W. Fan and W. Shi, *ACS Catal.* 2022, **12**, 1545-1557.
9. D. Xiao, X. Bao, D. Dai, Y. Gao, S. Si, Z. Wang, Y. Liu, P. Wang, Z. Zheng, H. Cheng, Y. Dai and B. Huang, *Adv. Mater.* 2023, **n/a**, 2304133.
10. Z. Zhou, Y.-n. Xie, L. Sun, Z. Wang, W. Wang, L. Jiang, X. Tao, L. Li, X.-H. Li and G. Zhao, *Appl. Catal. B Environ.* 2022, **305**, 121072.
11. Y. Xie, Z. Zhou, N. Yang and G. Zhao, *Adv. Funct. Mater.* 2021, **31**.
12. L. Gao, Z. Liu, J. Ma, L. Zhong, Z. Song, J. Xu, S. Gan, D. Han and L. Niu, *Appl. Catal. B Environ.* 2020, **261**, 118235.
13. H. Wang, C. Niu, W. Liu and S. Tao, *Appl. Catal. B Environ.* 2024, **340**, 123249.
14. S. Xie, H. Fu, L. Chen, Y. Li and K. Shen, *Sci. China Chem.* 2023, **66**, 2141-2152.